



The SLED project and the dynamics of coronal flux ropes

Jean-Marie Malherbe^a, Pierre Mein^a, Frédéric Sayède^b, Pawel Rudawy^c, Kenneth Phillips^d, Francis Keenan^e, Jan Rybák^f

^aObservatoire de Paris, LESIA, 92195 Meudon, France

^bObservatoire de Paris, GEPI, 92195 Meudon, France

^cAstronomical Institute, University of Wrocław, Poland

^dEarth Sciences Department, Natural History Museum, London SW75BD, United Kingdom

^eAstrophysics Research Centre, School of Mathematics and Physics, Queen's University Belfast, United Kingdom

^fAstronomical Institute, Slovak Academy of Sciences, 05960 Tatranská Lomnica, Slovakia

Received 1 May 2021; Received in final form -; Accepted -;

Available online -

Abstract

Investigations of the dynamics of the hot coronal plasma are crucial for understanding various space weather phenomena and making in-depth analyzes of the global heating of the solar corona. We present here numerical simulations of observations of siphon flows along loops (simple semi-circular flux ropes) to demonstrate the capabilities of the Solar Line Emission Dopplerometer (SLED), a new instrument under construction for imaging spectroscopy. It is based on the Multi-channel Subtractive Double Pass (MSDP) technique, which combines the advantages of filters and slit spectrographs. SLED will observe coronal structures in the forbidden lines of FeX 6374 Å and FeXIV 5303 Å, and will measure Doppler shifts up to 150 km s⁻¹ at high precision (50 m s⁻¹) and cadence (1 Hz). It is optimized for studies of the dynamics of fast evolving events such as flares or Coronal Mass Ejections (CMEs), as well as for the detection of high-frequency waves. Observations will be performed with the coronagraph at Lomnický Štít Observatory (LSO), and will also occur during total solar eclipses as SLED is a portable instrument.

© 2021 COSPAR. Published by Elsevier Ltd All rights reserved.

Keywords: Instrumentation ; Imaging spectroscopy ; Sun ; Coronal loops ; Dynamics

1. Introduction

Solar activity is the primary driver of space weather events which develop over short timescales (minutes) in solar flares and CMEs. Such events are highly dynamic and originate in the solar atmosphere from magnetic energy stored in active regions, sunspots (Borrero & Ichimoto, 2011) and coronal loops (Reale, 2014). Hence, direct velocity measurements are crucial for understanding the physics of such phenomena. In cold

layers (photosphere, chromosphere), Doppler observations are common; however, this is not the case at coronal temperatures.

The hot corona is imaged in the extreme ultraviolet (EUV) at 15 s maximum cadence by the Atmospheric Imaging Assembly (AIA) onboard the Solar Dynamics Observatory (SDO), at temperatures in the range 0.6 to 10.0 MK. STEREO and the Solar and Heliospheric Observatory (SOHO) use similar wavebands plus wide field, white light coronagraphs, while Solar Orbiter will soon offer EUV images. In parallel, ground-based coronagraphs provide observations at a much higher cadence, such as the SECIS instrument (Phillips et al., 2000), working in the green line of FeXIV 5303 Å. The corona has also been observed during total solar eclipses in visible emission lines (Rudawy et al., 2019), as well as in infrared (IR) lines (Habbal et al., 2011).

Email addresses: Jean-Marie.Malherbe@obspm.fr (Jean-Marie Malherbe), Pierre.Mein@club-internet.fr (Pierre Mein), Frederic.sayede@obspm.fr (Frédéric Sayède), rudawy@astro.uni.wroc.pl (Pawel Rudawy), kennethjphillips@yahoo.com (Kenneth Phillips), f.keenan@qub.ac.uk (Francis Keenan), rybak@astro.sk (Jan Rybák)

Imaging instruments cannot measure plasma velocities, and for this tunable filters or spectrographs are required. LASCO/C1 onboard SOHO was able to scan the green (FeXIV) and red (FeX) lines with a Fabry P erot filter (Brueckner et al., 1995). Mierla et al. (2008) studied velocities in the quiet corona, but it was not possible to access the velocities of fast events such as CMEs, due to the long time needed to scan the profiles. Singh et al. (2002) have characterized the coronal green (FeXIV 5303  ) and red (FeX 6374  ) emission lines using narrow slit spectroscopy. Spectra of the green line were also recorded by Sakurai et al. (2002). Livingston et al. (1980) and Singh et al. (1982) introduced multi-slit spectroscopy during the total solar eclipse of 16 February 1980 to measure velocities. The Coronal Multi-channel Polarimeter (CoMP, Tomczyk et al. (2008)) is a ground-based instrument working in the IR lines of FeXIII (10747   and 10798  ). CoMP can record velocities (and magnetic fields) with 15 s temporal resolution; it was used, for instance, to study Alfv en waves (Tomczyk et al., 2007) or the dynamics of CMEs (Tian et al., 2013).

The SLED instrument described in this paper will allow the measurement of line-of-sight (LOS) velocities in the coronal green and red lines, in a 2D field of view (FOV) and at high cadence (1 Hz), by combining the advantages of spectroscopy and tunable filters. Section 2 explains the principles of the imaging spectroscopy concept used by the SLED, while Section 3 summarizes the optical design. Section 4 presents the main scientific goals of the instrument and simulations of its capabilities are detailed in Section 5.

2. The Multichannel Subtractive Double Pass (MSDP) technique

SLED is a compact version of the MSDP imaging-spectrographs; the principle was first described by Mein (1977), and has been upgraded many times over the last decades on several telescopes (Mein et al., 2021). The layout of MSDP is shown in Figure 1 with a sample set of past observations. It is an imaging double pass spectrograph using a 2D rectangular entrance window (F1) and a slicer located in the focal plane of the spectrum (F2), after a first pass on the grating. The slicer selects N channels (beam-splitting) and realigns the N channels (beam-shifting) before the subtraction of the dispersion by the second pass on the grating. The output of the MSDP (F3) is composed of N contiguous spectra-images ($N = 9$ in Figure 1). There is a constant wavelength step between each spectra-image, but within each, the wavelength varies linearly along the x -direction. Data cubes (x, y, λ) of the whole FOV are extracted from a single exposure. Hence, the MSDP combines the advantages of filters and spectroscopy. The 2D FOV depends on the focal length of the telescope and the size of the window (F1), while the spectral resolution depends on the focal length of the spectrograph and the slicer parameters. The cadence is only limited by the photon flux and the detector speed.

The SLED/MSDP parameters are optimized for coronal lines (0.3   resolution), high velocities ($N = 24$), the size of

active regions (150'' \times 1000'' FOV) and time-scales involved in fast events or high-frequency waves (1 s).

3. The SLED optical design

The SLED has spectral resolution and wavelength range of respectively 0.28   and 6.5   (24×0.28  ) for the FeXIV 5303   forbidden line. These parameters are convenient for coronal line widths (typically 0.8   FWHM) and large Doppler shifts ($\pm 100 \text{ km s}^{-1} \approx \pm 2.0$  ).

The optical path of the SLED spectrograph is schematized in Figure 2, where the letters L and M refer to lenses and plane mirrors, respectively. The set of four lenses L1 to L4 acts as a collimator. Optical components of the spectrograph are:

- F1: the rectangular entrance window (4.4 mm x 31.0 mm) located at the spectrograph focus.
- The first pass (light dispersion): F1, L1, M1, L2, M2, L3, L4, grating, L4, L3, M2, L2, M1, L1, M3, slicer (F2).
- F2: 24 channels slicer located in the spectrum, made of 24 beam-splitting micro-mirrors and 24 associated beam-shifting mirrors.
- The second pass (subtractive dispersion): slicer (F2), M4, M5, L1, M1, L2, M2, L3, L4, grating, L4, L3, M2, L2, M1, L1.
- The reduction optics to the detector: M6, field lens, M7 and camera lens (0.2 magnification).
- F3: the Andor Zyla camera (5.5 Mpixels sCMOS detector, 2560 \times 2160 format, 6.5 micron square pixels) recording the 24 channel spectra-images with 2.1'' spatial sampling.

The optical combination of four lenses (L1, L2, L3, L4) acts as a collimator (2.0 m equivalent focal length) with folding mirrors (M1, M2), while the grating is 62  blazed and 79 grooves/mm ruled. Orders are selected by filters (order 42 for FeXIV), and the resolution is $R = 19000$, with dispersion $D = 1.43 \text{ mm}/\text{ }$ (for FeXIV). The wavelength sampling (0.28  ) is the ratio S/D , where $S = 0.4 \text{ mm}$ is the micro-mirror step of the slicer. On exit, the camera lens (100 mm focal length) has a magnification factor of 0.2. More details are given in Mein et al. (2021).

There is a major difference between SLED/MSDP and conventional integral field spectrographs such as the GREGOR Infrared Spectrograph (GRIS, Vega Reyes et al. (2016)) and MUSICa for the future European Solar Telescope (Calcines et al., 2013). Specifically, SLED has a large variation of its spectral window coverage as a function of the FOV position in the direction parallel to the dispersion. In the centre of the FOV, the spectral range provided by the 24 channels is $[-3.25 \text{  }, +3.25 \text{  }]$, corresponding to velocities up to 160 km s^{-1} . Towards the FOV edges, the spectral range keeps the same width (6.5  ) but is shifted from $[-4.8 \text{  }, +1.7 \text{  }]$ to $[-1.7 \text{  }, +4.8 \text{  }]$ respectively from the left to the right side, where velocities up to 75 km s^{-1} can still be determined. This 3.1   shift between both sides

is the ratio W/D , where $W = 4.4$ mm is the width of the 2D entrance window.

4. The scientific goals of the SLED

The SLED has two main goals owing to its capability to produce Dopplergrams at high temporal resolution.

4.1. Dynamic events of solar activity

SLED will observe the dynamics of coronal flux ropes and loops in active regions, flares, and CMEs, which drive solar-terrestrial interactions. It will study the plasma motions (Doppler shifts) inside hot structures (1 to 2 MK) at high cadence (1 Hz). These measurements could be combined with EUV intensities obtained at lower cadence by AIA onboard SDO in several lines emitted by plasma at temperatures in the range 0.6 to 10 MK. SLED will impose new constraints on models describing the dynamics of hot loops and their temporal evolution. The instrument will be available before the forthcoming solar maximum (cycle 25), when major events are expected to occur.

4.2. Coronal heating

Processes involved in the coronal heating are not yet fully understood (Klimchuk, 2006). The main plausible mechanisms fall into two categories: heating by numerous and concentrated magnetic reconnections (nano-flares), or the dissipation of Alfvén or MHD waves in coronal loops. Observations with CoMP (Tomczyk et al., 2007) revealed Alfvén-type wave motions of low frequency (peaking at 3.5 mHz) around active regions at the limb. However, their energy is too small to explain the heating, for which higher frequency waves are likely to be involved. Owing to telemetry limitations of satellites, a search for high-frequency waves was undertaken with ground-based instruments in fast imagery mode through narrow-band filters in the visible FeXIV or FeX lines. Samanta et al. (2016) searched for high frequency oscillations (0.1 Hz) using multi-slit spectroscopy of these two lines, observed simultaneously during the eclipse of 11 July 2010. Several campaigns were organized with SECIS (Rudawy et al. (2004), Rudawy et al. (2010), Rudawy et al. (2019)), but the short period fluctuations were questionable in terms of waves. For this reason, the SLED will investigate oscillations using Doppler measurements.

5. Simulation of the SLED capabilities

The core of the SLED is the 24 channel-slicer designed for F/30 beam. It is built for 0.20 m diameter/6.0 m equivalent focal length telescopes, such as the high-altitude Lomnický Štít Observatory (LSO) coronagraph (Lexa, 1963). However, the SLED will also be used for total eclipse observations, as it is a portable spectrograph. The FOV is compatible with the typical size of coronal active region loops (10^5 km).

In Figure 3 the wavelength response of the 24 channels in terms of Doppler shifts (converted to velocities, positive for blue shifts) is displayed for the coronal green and red lines.

Table 1. Precision of velocity measurements (IP = inflexion points).

Chord length (\AA)	RMS error (km/s)
0.56	0.25
0.63	0.11
0.70 ($\approx IP$)	0.05
0.77 ($\approx FWHM$)	0.17
0.84 ($\approx FWHM$)	0.23

The channels are not monochromatic, as the wavelength varies in the x-direction of the 2D FOV. Velocities up to 75 km s^{-1} can be determined at all points in the FOV. However, velocities of the order of the local sound speed (150 km s^{-1}) can be measured near the FOV centre. For the green line, the maximum velocity is given by the relation $|v_{max}| = -1.17|x| + 163 \text{ km s}^{-1}$ where x is the abscissa (") along the FOV. Hence, the SLED is ideally suited to observations of highly dynamic phenomena during solar activity.

In order to demonstrate the capabilities of the SLED to restore LOS velocities, we used the results of the simple model of Cargill & Priest (1980). It is a steady-state and adiabatic siphon flow in a semi-circular coronal magnetic loop with constant cross-section (see Figure 6a of their paper). They suggested several possible regimes, such as subsonic, transonic and supersonic flows with shocks (when the local Mach number M exceeds unity). Assuming observations at the limb, we explored different view angles of the loop with respect to the line-of-sight, shown in Figure 4. The response of the SLED in terms of spectra images is simulated in Figure 5 in the case of a subsonic siphon flow observed in the FeXIV green line with a Gaussian profile of 0.8 \AA FWHM.

From the SLED spectra image, such as that in Figure 5, we restored LOS velocities of subsonic and supersonic shocked flows seen through a rectangular 2D FOV either tangential or orthogonal to the limb. The SLED samples the line profiles with a 0.28 \AA step by the transfer functions of Figure 3. We used a two-pass cubic interpolation to optimize the reconstruction of line profiles. LOS velocities were then computed using the bisector technique, in which we detect the middle position of a chord of 0.70 \AA width, corresponding to the distance between the inflexion points. This choice minimizes errors in the velocity measurements. We found an excellent precision of 50 m s^{-1} RMS, so that the SLED restorations of Figures 6 and 8 are indistinguishable from the LOS velocities of the input model. Table 1 shows the RMS interpolation error for different chords: it clearly indicates that inflexion points provide the best precision (the slope of the profiles is maximum there). We have also simulated the effect of the photon noise: it must be considered when the signal to noise ratio is smaller than about 100. We estimate (from SECIS extrapolation) that it should be 50 for the 1 Hz cadence necessary to study high frequency waves, and above 100 for moderate frame rates. Asymmetrical profiles can also affect the precision, for instance in the case of velocity gradients along the line of sight.

Figure 6 shows the restoration of LOS velocities (using the inflexion points) in the case of high-speed supersonic shocked flows ($M = 1.5$) when the (long) y -direction of the rectangular FOV is orthogonal to the limb, for the various view angles of Figure 4. The curvilinear abscissa s along the flux rope is normalized to 1, and the shock is located at $s = 0.7$. SLED can measure LOS velocities up to the sound speed when the shocked region is close to the centre of the FOV in the x -direction. Within this orientation, the radius of the loop cannot exceed 55000 km (half-width of the FOV). Figure 7 displays the precision of the velocity restoration along the loop for 45° view angle; the best result is obtained when Doppler shifts are measured near the inflexion points of spectral lines. Oscillations correspond to interpolation errors occurring along the loop, because the sampling wavelengths of the profiles vary according to the LOS velocities and the x -abscissae in the FOV.

Alternatively, Figure 8 shows the restoration of LOS velocities when the (long) y -direction of the FOV is tangential to the limb, for the various angles of Figure 4. Within this orientation, the maximum radius of the loop is 110000 km (the width of the FOV). In the left panel of the figure, we used the subsonic model, so that LOS velocities are easily restored everywhere in the FOV. However, in the right panel, we used the supersonic shocked flow model ($M = 1.5$), and the highest LOS velocities, now close to the sides of the FOV, can no longer be properly recovered for all angles. Hence, the FOV orientation has to be considered when large radial velocities are suspected in coronal structures.

6. Conclusions

The Solar Line Emission Dopplerometer (SLED) is a new instrument for studies of the dynamics of coronal structures in the forbidden lines of FeX and FeXIV. Dopplergrams providing line-of-sight velocities will be delivered at high cadence (1 Hz) for a large FOV at the limb ($150'' \times 1000''$, $2.1''$ pixel sampling). Plasma motions can be investigated during fast-evolving events such as flares or CMEs, and high-frequency oscillations relevant to coronal heating will be searched. Full line profiles (0.28 \AA resolution) will be available everywhere in the 2D FOV, owing to an imaging spectroscopy technique which is faster than most tunable filters or slit spectrographs. However, the spectral window is not the same for different abscissae in the FOV, but has a constant width. SLED will complement spectroscopic instruments operating mainly in IR lines, such as CoMP or the future VELC onboard Aditya-L1 (Raj Kumar et al., 2018). It will monitor the coronal activity of cycle 25 at Lomnický Štít Observatory, but it could also observe total solar eclipses, such as the event of 8 April 2024 (North America).

7. Acknowledgments

We are indebted to the two referees for helpful comments and suggestions. We are grateful for financial support to the Institut National des Sciences de l'Univers (INSU/CNRS), the

University of Wrocław, the UK Science and Technology Facilities Council (STFC), the Leverhulme Trust via grant RPG-2019-371, and Queen's University Belfast. J.R. acknowledges support by the Science Grant Agency project VEGA 2/0048/20 (Slovakia).

References

- Borrero, J. M., & Ichimoto, K. (2011). Magnetic Structure of Sunspots. *Living Reviews in Solar Physics*, 8(1), 4. doi:10.12942/lrsp-2011-4. arXiv:1109.4412.
- Brueckner, G. E., Howard, R. A., Koomen, M. J., Korendyke, C. M., Michels, D. J., Moses, J. D., Socker, D. G., Dere, K. P., Lamy, P. L., Llebaria, A., Bout, M. V., Schwenn, R., Simnett, G. M., Bedford, D. K., & Eyles, C. J. (1995). The Large Angle Spectroscopic Coronagraph (LASCO). *Solar Phys.*, 162(1-2), 357–402. doi:10.1007/BF00733434.
- Calcines, A., López, R. L., & Collados, M. (2013). MuSICa: the Multi-Slit Image Slicer for the est Spectrograph. *Journal of Astronomical Instrumentation*, 2(1), 1350009. doi:10.1142/S2251171713500098.
- Cargill, P. J., & Priest, E. R. (1980). Siphon Flows in Coronal Loops - Part One - Adiabatic Flow. *Solar Phys.*, 65(2), 251–269. doi:10.1007/BF00152793.
- Habbal, S. R., Cooper, J., Daw, A., Ding, A., Druckmuller, M., Esser, R., Johnson, J., & Morgan, H. (2011). Exploring the Physics of the Corona with Total Solar Eclipse Observations. *arXiv e-prints*, (p. arXiv:1108.2323). arXiv:1108.2323.
- Klimchuk, J. A. (2006). On Solving the Coronal Heating Problem. *Solar Phys.*, 234(1), 41–77. doi:10.1007/s11207-006-0055-z. arXiv:astro-ph/0511841.
- Lexa, J. (1963). New coronagraph of the Astronomical Observatory of the Slovak Academy of Sciences at Skalnaté Pleso. *Bulletin of the Astronomical Institutes of Czechoslovakia*, 14, 107.
- Livingston, W., Harvey, J., Doe, L. A., Gillespie, B., & Ladd, G. (1980). The Kitt-Peak Coronal Velocity Experiment. *Bulletin of the Astronomical Society of India*, 8, 43.
- Mein, P. (1977). Multi-channel subtractive spectrograph and filament observations. *Solar Phys.*, 54(1), 45–51. doi:10.1007/BF00146423.
- Mein, P., Malherbe, J. M., Sayède, F., Rudawy, P., Phillips, K. J. H., & Keenan, F. P. (2021). Four Decades of Advances from MSDP to S4I and SLED Imaging Spectrometers. *Solar Phys.*, 296(2), 30. doi:10.1007/s11207-021-01766-9. arXiv:2101.03918.
- Mierla, M., Schwenn, R., Teriaca, L., Stenborg, G., & Podlipnik, B. (2008). Analysis of the Fe X and Fe XIV line width in the solar corona using LASCO-C1 spectral data. *Astron. Astrophys.*, 480(2), 509–514. doi:10.1051/0004-6361/20078329. arXiv:0903.0496.
- Phillips, K. J. H., Read, P. D., Gallagher, P. T., Keenan, F. P., Rudawy, P., Rimpolt, B., Berlicki, A., Buczylo, A., Diego, F., Barnsley, R., Smartt, R. N., Pasachoff, J. M., & Babcock, B. A. (2000). SECIS: The Solar Eclipse Coronal Eclipse Imaging System. *Solar Phys.*, 193, 259–271. doi:10.1023/A:1005274827585.
- Raj Kumar, N., Raghavendra Prasad, B., Singh, J., & Venkata, S. (2018). Optical design of visible emission line coronagraph on Indian space solar mission Aditya-L1. *Experimental Astronomy*, 45(2), 219–229. doi:10.1007/s10686-017-9569-7.
- Reale, F. (2014). Coronal Loops: Observations and Modeling of Confined Plasma. *Living Reviews in Solar Physics*, 11(1), 4. doi:10.12942/lrsp-2014-4.
- Rudawy, P., Phillips, K. J. H., Buczylo, A., Williams, D. R., & Keenan, F. P. (2010). Search for Rapid Changes in the Visible-Light Corona during the 21 June 2001 Total Solar Eclipse. *Solar Phys.*, 267(2), 305–327. doi:10.1007/s11207-010-9647-8. arXiv:1009.5205.
- Rudawy, P., Phillips, K. J. H., Gallagher, P. T., Williams, D. R., Rimpolt, B., & Keenan, F. P. (2004). Search for 1-10 Hz modulations in coronal emission with SECIS during the August 11, 1999 eclipse. *Astron. Astrophys.*, 416, 1179–1186. doi:10.1051/0004-6361/20031737.
- Rudawy, P., Radziszewski, K., Berlicki, A., Phillips, K. J. H., Jess, D. B., Keys, P. H., & Keenan, F. P. (2019). A Search for High-Frequency Coronal Brightness Variations in the 21 August 2017 Total Solar Eclipse. *Solar Phys.*, 294(4), 48. doi:10.1007/s11207-019-1428-4. arXiv:1903.06076.

- Sakurai, T., Ichimoto, K., Raju, K. P., & Singh, J. (2002). Spectroscopic Observation of Coronal Waves. *Solar Phys.*, 209(2), 265–286. doi:10.1023/A:1021297313448.
- Samanta, T., Singh, J., Sindhuja, G., & Banerjee, D. (2016). Detection of High-Frequency Oscillations and Damping from Multi-slit Spectroscopic Observations of the Corona. *Solar Phys.*, 291(1), 155–174. doi:10.1007/s11207-015-0821-x. arXiv:1511.07160.
- Singh, J., Sakurai, T., Ichimoto, K., Suematsu, Y., & Takeda, A. (2002). Spectroscopic Studies of the Solar Corona II. Properties of Green and Red Emission Lines in Open and Closed Coronal Structures. *Pub. Astron. Soc. Japan*, 54, 793–806. doi:10.1093/pasj/54.5.793.
- Singh, J., Saxena, A. K., & Bappu, M. K. V. (1982). Eclipse observations of coronal emission lines. I - Forbidden Fe X 6374 Å profiles at the eclipse of 16 February 1980. *Journal of Astrophysics and Astronomy*, 3, 249–266. doi:10.1007/BF02714865.
- Tian, H., Tomczyk, S., McIntosh, S. W., Bethge, C., de Toma, G., & Gibson, S. (2013). Observations of Coronal Mass Ejections with the Coronal Multichannel Polarimeter. *Solar Phys.*, 288(2), 637–650. doi:10.1007/s11207-013-0317-5. arXiv:1303.4647.
- Tomczyk, S., Card, G. L., Darnell, T., Elmore, D. F., Lull, R., Nelson, P. G., Streaender, K. V., Burkepile, J., Casini, R., & Judge, P. G. (2008). An Instrument to Measure Coronal Emission Line Polarization. *Solar Phys.*, 247(2), 411–428. doi:10.1007/s11207-007-9103-6.
- Tomczyk, S., McIntosh, S. W., Keil, S. L., Judge, P. G., Schad, T., Seeley, D. H., & Edmondson, J. (2007). Alfvén Waves in the Solar Corona. *Science*, 317(5842), 1192. doi:10.1126/science.1143304.
- Vega Reyes, N., Esteves, M. A., Sánchez-Capuchino, J., Salaun, Y., López, R. L., Gracia, F., Estrada Herrera, P., Grivel, C., Vaz Cedillo, J. J., & Colados, M. (2016). Opto-mechanical design of an image slicer for the GRIS spectrograph at GREGOR. In R. Navarro, & J. H. Burge (Eds.), *Advances in Optical and Mechanical Technologies for Telescopes and Instrumentation II* (p. 99125P). volume 9912 of *Society of Photo-Optical Instrumentation Engineers (SPIE) Conference Series*. doi:10.1117/12.2232615.

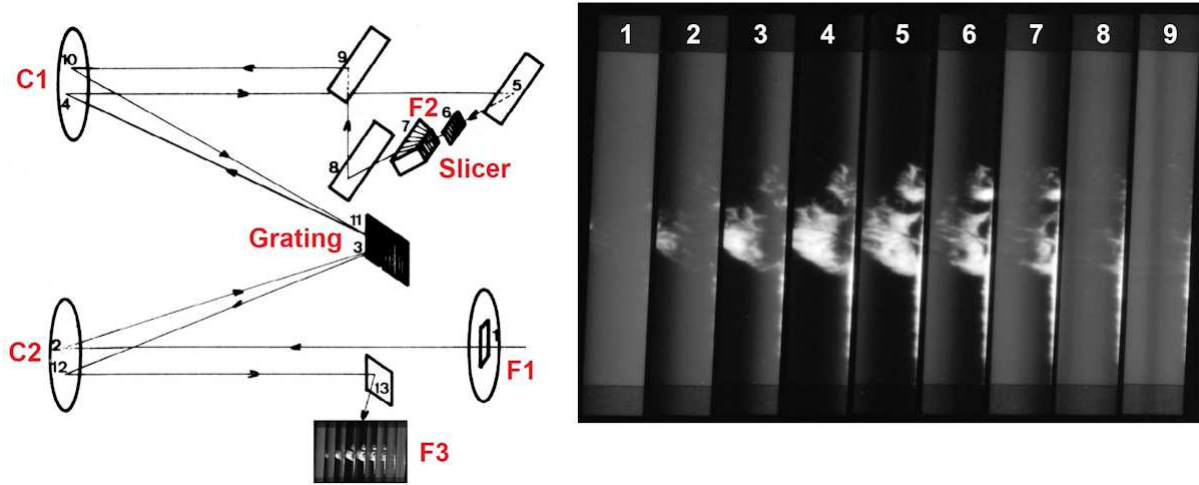


Fig. 1. Left: principle of MSDP spectrographs. F1 = entrance window. F2 = spectrum. F3 = output with N spectra-images. C1 and C2 are collimators. The numbers (1 to 13) indicate the light path. Right: an example of a prominence at the limb observed in H α line with N = 9 channels.

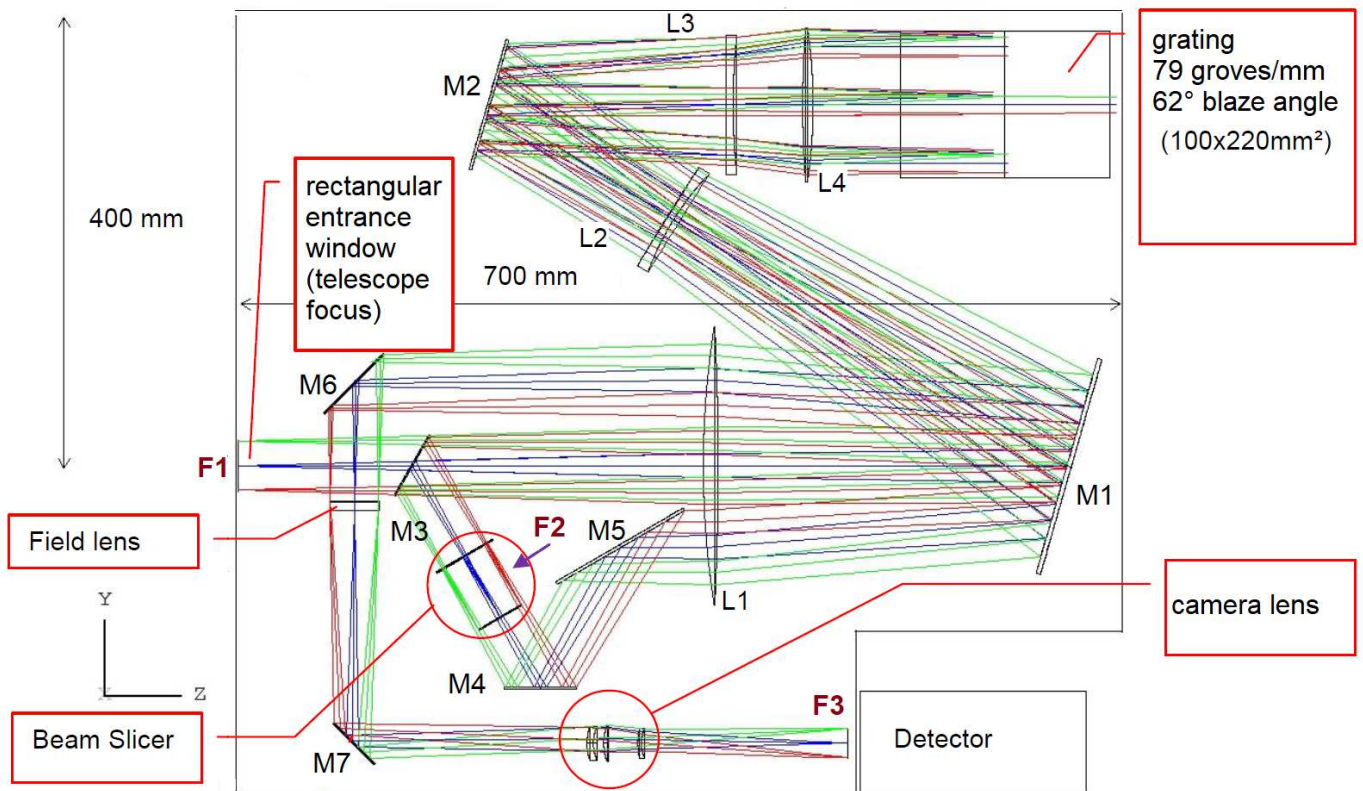


Fig. 2. The optical design of the SLED spectrograph. The layout is described in detail in Section 3.

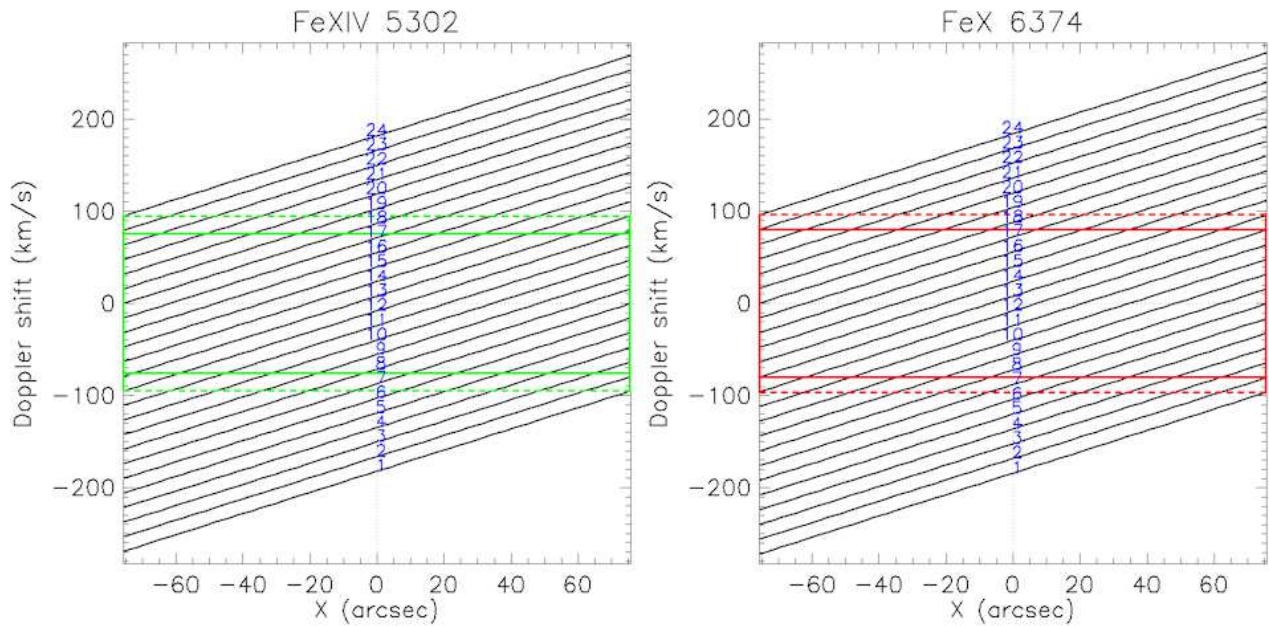


Fig. 3. Wavelength transmissions of the 24 channels (numbers 1 - 24) of the SLED for the FeXIV green line (left) and the FeX red line (right). Abscissa: x direction along the 2D FOV ("); ordinate: wavelength converted to LOS velocities (km s^{-1}). The solid/dashed rectangles indicate the velocity range available over the full FOV, provided by measurements respectively at the inflexion points or peaks of the emission profiles.

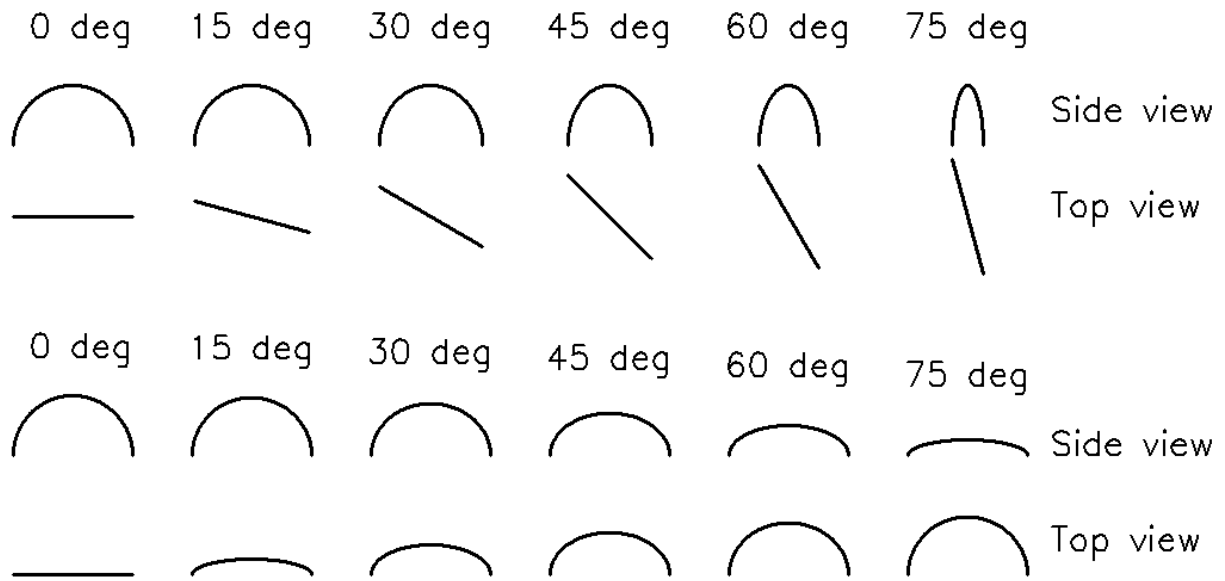


Fig. 4. Semi-circular magnetic flux tube seen at the limb under various conditions and angles. Top: the plane of the loop is orthogonal to the solar surface, but is rotated with respect to the plane of the sky (except for 0°). Bottom: the plane of the loop is inclined with respect to the local vertical (except for 0°).

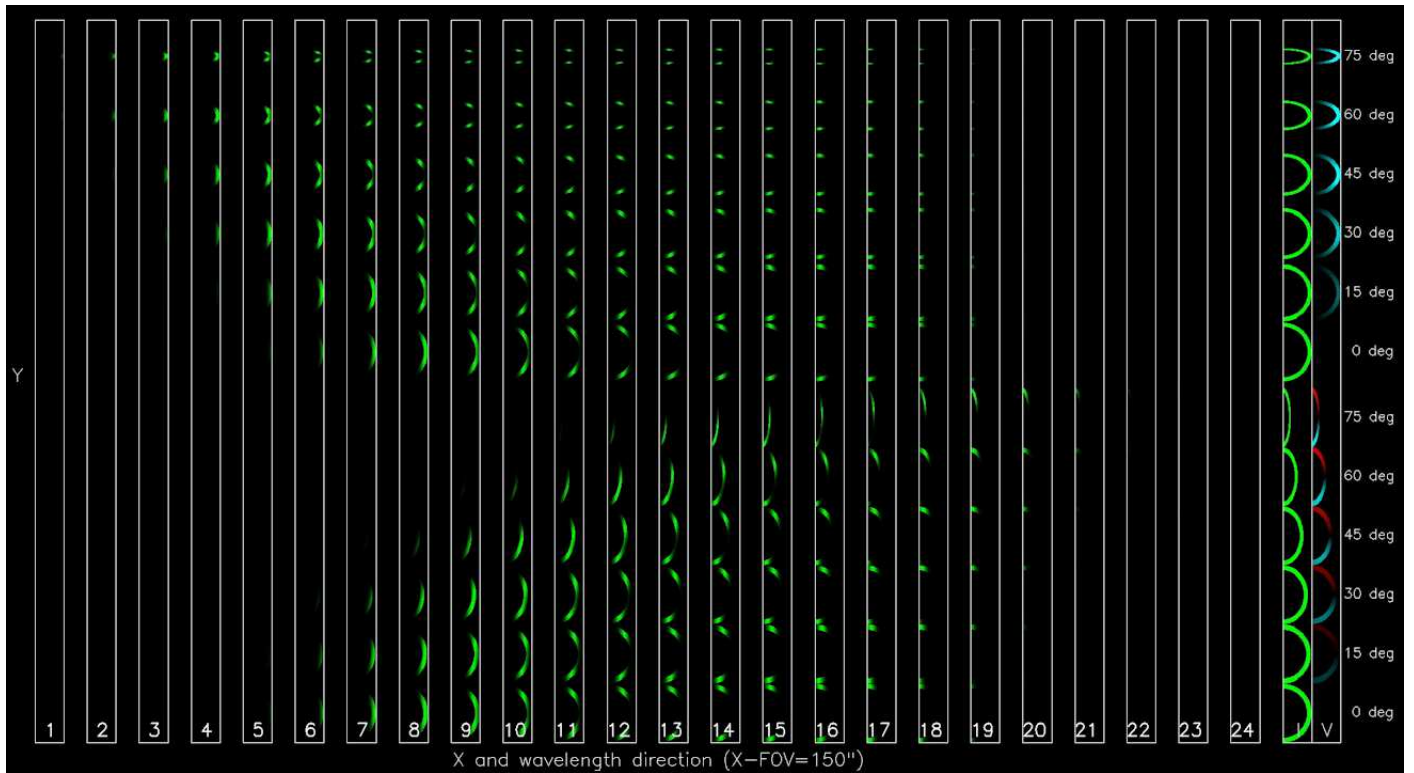


Fig. 5. Spectra images of the SLED in the case of a loop with subsonic flows observed at the limb under the different viewing conditions of Figure 4. The 24 channels are shown together with the input intensity (I) and LOS velocities (V) derived from the siphon flow model and the various angles. Blue/red colour are coding blue and red shifts of the model.

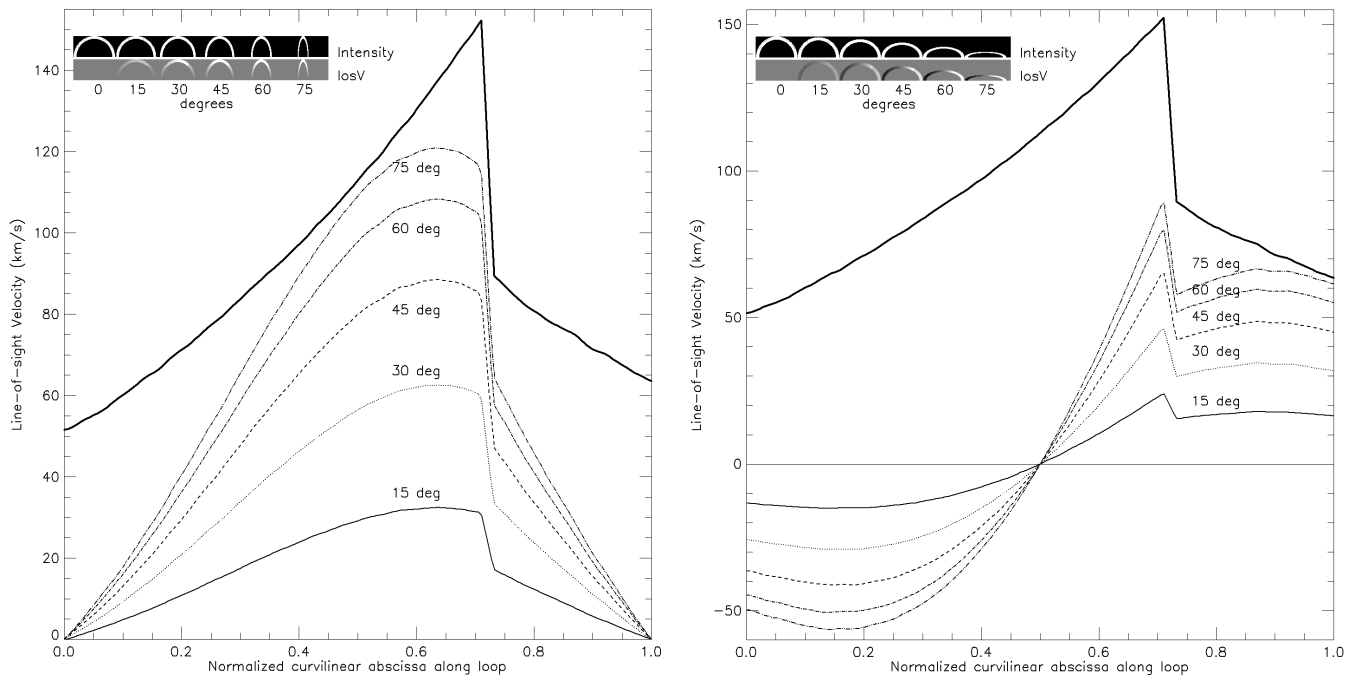


Fig. 6. Restoration of LOS velocities with the FOV orthogonal to the limb. Abscissa: normalized curvilinear coordinate s along the loop. The thick line represents the velocities of the input model, which are tangential to the semi-circular loop (shock at $s = 0.7$). The two panels correspond to the two sets of view angles of Figure 4. The thin, dotted, dashed and dot-dashed lines are respectively for 15° , 30° , 45° , 60° and 75° view angles.

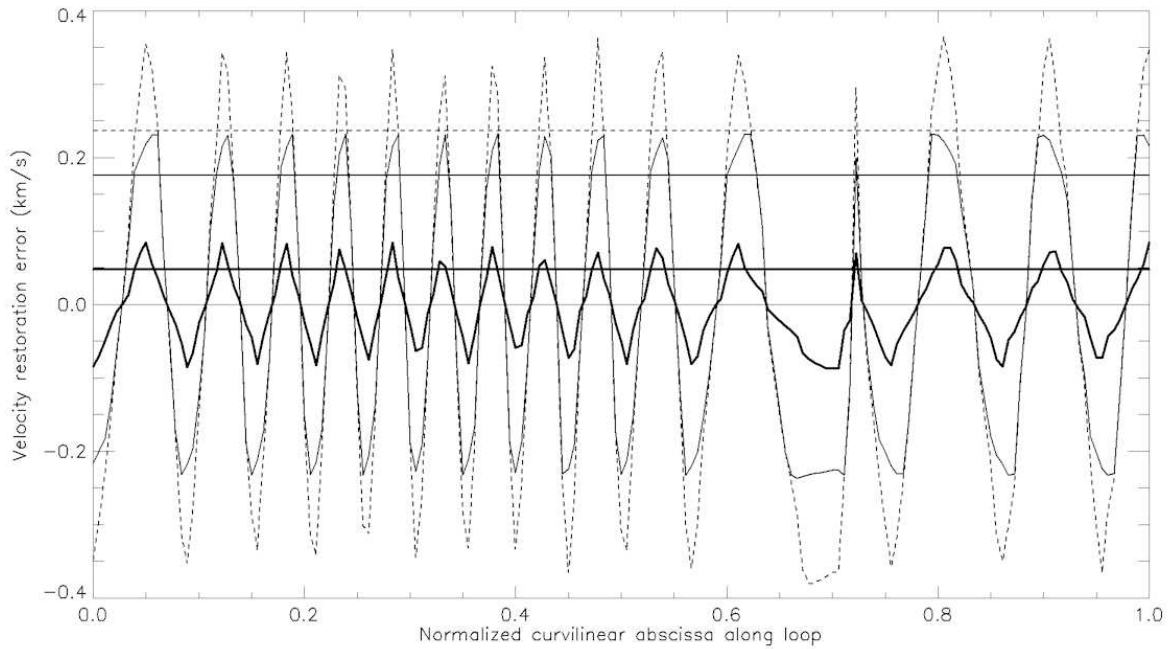


Fig. 7. Precision (km s^{-1}) of the restoration of LOS velocities shown in Figure 6 for 45° view angle. Abscissa: normalized curvilinear coordinate s along the loop. The thick, thin and dashed lines represent respectively the error for chords of 0.70 \AA (inflection points), 0.77 \AA and 0.84 \AA (FWHM). Associated horizontal lines give the RMS error level. The shock is located at $s = 0.7$.

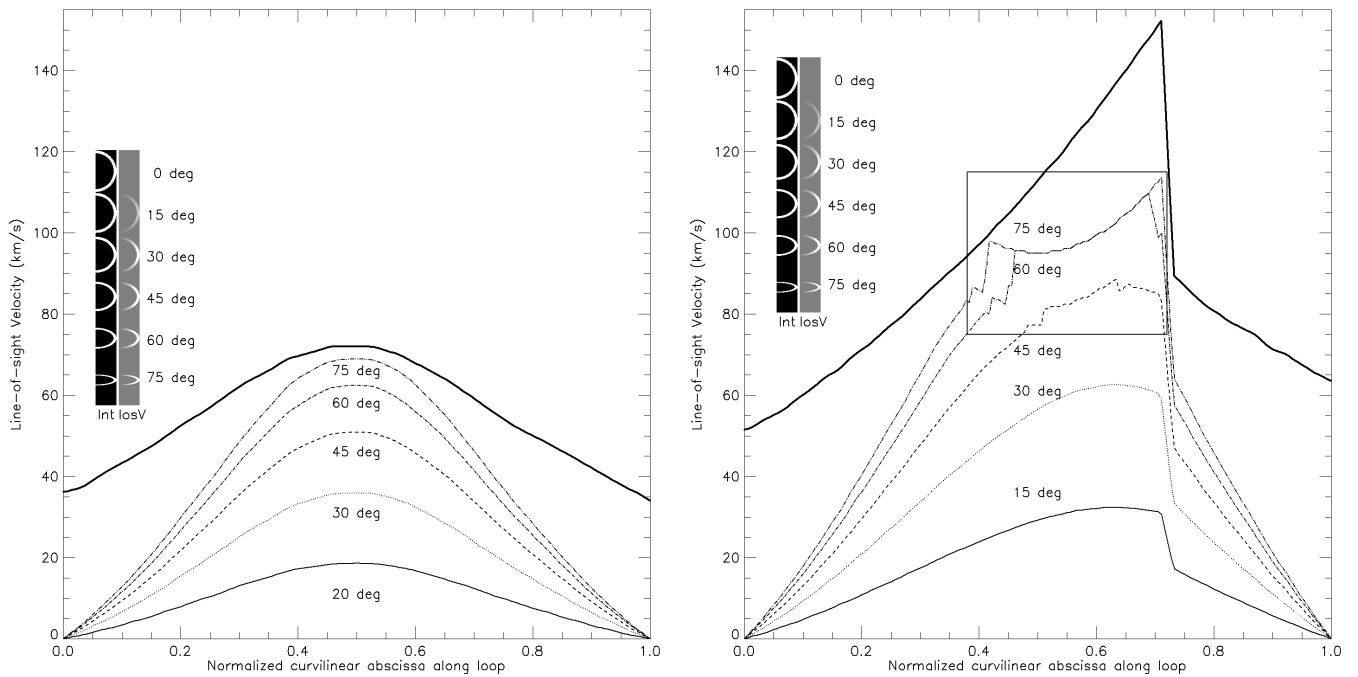


Fig. 8. Restoration of LOS velocities with the FOV tangential to the limb. Abscissa: normalized curvilinear coordinate s along the loop. The thick line represents the velocities of the input model, which are tangential to the semi-circular loop. The thin, dotted, dashed and dot-dashed lines are respectively for 15° , 30° , 45° , 60° and 75° view angles. Left: subsonic model. Right: shocked model (shock at $s = 0.7$); the box indicates a saturation phenomenon happening when the plane of the loop is strongly rotated with respect from the plane of the sky.